International Journal of Heat and Mass Transfer 237 (2025) 126448

Contents lists available at ScienceDirect

International Journal of Heat and Mass Transfer

journal homepage: www.elsevier.com/locate/ijhmt

Numerical investigation on droplet lateral movement in post-dryout region

Zihan Xia *, Xu Cheng

Institute for Applied Thermofluidics (IATF), Karlsruhe Institute of Technology (KIT), Kaiserstrasse 12, Karlsruhe 76131, Germany

ARTICLE INFO

Keywords:
Discrete particle method
Droplet lateral movement
Droplet deposition
Evaporation effect

ABSTRACT

This paper presents a numerical study of droplet lateral movement and droplet deposition behaviors in the post-dryout region using the Discrete Particle Model (DPM) in ANSYS FLUENT. The investigation focuses on the analysis of droplet lateral movement, including single droplet trajectory, the statistic distribution and average value of droplets radial velocity, and droplet transverse between central and near wall regions. The single droplet trajectory shows the droplet dynamic behavior in the near wall region vividly. The droplet radial velocities are plotted as histogram to display the droplets statistic characteristics. The average value of droplets radial velocities toward the wall are plotted along the radial distance. In addition, to quantitatively display the size and evaporation effect on droplet deposition, three new parameters presenting overall movement behavior, i.e. droplet deposition mass flux, droplet deposition velocity as well as droplet entrainment velocity are introduced and derived from the CFD results. The comparison of results with varying initial droplet size indicates that droplets with smaller sizes exhibit higher average velocities toward the wall. A smaller initial droplet size leads to a higher deposition velocity, lower entrainment velocity, and thus a higher droplet deposition mass flux. The histogram of droplet radial velocities reveals that the droplet evaporation significantly reduces the number of droplets with small radial velocities toward the wall, resulting in a decrease in overall droplet deposition mass flux. Furthermore, through the comparison of overall movement behavior parameters, evaporation not only inhibits droplet motion toward the wall but also noticeably enhances droplet movement away from the wall. This inhibition effect on droplet deposition and enhancement effect on droplet entrainment become more pronounced with increasing evaporation intensity.

1. Introduction

In boiling heat exchange systems, when the heat flux of heated surface exceeds the critical heat flux, the liquid film in annular flow disappears, causing a sudden rise in wall temperature, a phenomenon known as dryout. The region following the onset of dryout is referred as post-dryout region, where the flow pattern is figured out as the dispersed flow film boiling (DFFB). The post-dryout heat transfer determines the peak temperature of heated surface and the duration of high temperature, which has great significance to the integrity of heated surface. Therefore, this topic has been extensively researched over the past several decades. The complexity of accurately predicting wall temperatures under varying conditions continues to challenge researcher, new studies emerging to refine and improve prediction models for better accuracy across different scenarios [1–4]. In the post-dryout region, the wall superheating is typically very high, often reaching several hundred degrees Celsius. In the dispersed flow, the liquid is entrained in the vapor as discrete droplets. The wall transfers heat to the vapor, leading to an increase in vapor superheating. The droplets entrained in the vapor flow absorb heat from superheated vapor, which slows down the process of vapor superheating, thus affecting the developing process of wall temperature after dryout. The droplets also tend to move to the wall, deposit on the wall and transfer heat directly from the wall, further contributing to wall cooling. Droplet parameters, such as droplet size, velocity, and distribution, are critical factors in post-dryout heat transfer. Numerous studies have been conducted to better understand droplet behaviors. For instance, Yang et al. [5] investigated the contact heat transfer behavior of droplet impact on a hot surface, combining experimental data with numerical simulations. Saini and Bolotnov [6] used direct numerical simulation (DNS) to model dispersed droplets, emphasizing the effects of droplet presence and the influence of varying Weber numbers on turbulence in the surrounding steam. Chen et al. [7] performed experimental analyses on the transient characteristics of droplets in the dispersed film boiling (DFFB) regime during the reflood phase, with a particular focus on droplet size and distribution.

The mechanistic models of post-dryout include heat transfer processes of wall to vapor, vapor to droplet and wall to droplet are

* Corresponding author.
E-mail addresses: zihan.xia@kit.edu (Z. Xia), xu.cheng@kit.edu (X. Cheng).

https://doi.org/10.1016/j.ijheatmasstransfer.2024.126448
Received 2 October 2024; Received in revised form 1 November 2024; Accepted 11 November 2024
Available online 18 November 2024
0017-9310/© 2024 The Authors. Published by Elsevier Ltd. This is an open access article under the CC BY-NC license (http://creativecommons.org/licenses/by-nc/4.0/).

Nomenclature

A_{cont}: the contact area of droplets and wall (m^2)
C_d: droplet concentration (kg/ m^3)
C_D: drag coefficient
C_f: wall friction coefficient
$c_{p,g}$: heat capacity of the vapor (J/kg·K)
$c_{p,d}$: heat capacity of the droplet (J/kg·K)
D_0 : droplet diameter before impact (m)
D_{max}: droplet maximum spreading diameter (m)
$d_{p,0}$: droplet diameter at injection(m)
d_p: droplet diameter (m)
d_t: tube diameter (m)
$\overrightarrow{F}$: additional force (N)
f : constant with the default value of 0.4
G_d: mass flow rate of the droplets(kg/s)
$G_{d,0}$: initial mass flow rate of the droplets(kg/s)
h_{lg}: latent heat (J/kg)
H_{wd} : droplet center-point to wall distance(m)
k_d: droplet deposition velocity (m/s)
k_l : thermal conductivity of liquid droplet (w/m-K)
k : turbulent kinetic energy (m^2/ s^2)
m_d: droplet mass(kg)
$\dot{m}_d$: droplet mass flux (kg /m^2•s)
Pr : Prandtl number of the vapor
r_c: separation line of central region and near-wall region(m)
Re: Reynolds number of continuous phase
Re_d: Relative Reynolds number
Re_l: Reynolds number of dispersed phase
t_d: droplet and wall contact time (s)
T_d: droplet temperature (K)
T_g: temperature of vapor (K)
T_w: wall temperature (K)
t : time (s)
Δt: time step(s)
$\overrightarrow{u}_g$: instantaneous vapor velocity (m/s)
$\overline{u}_g$: time average vapor velocity (m/s)
u_g : component of actual vapor velocity in u direction(m/s)
$\overrightarrow{u}_d$: droplet velocity (m/s)
u', v',w': fluctuation velocity in u, v, w (m/s)
u^*: friction velocity
We : Impact Weber number
x_d: droplet position (m)
n: droplet at old location
$n+1$: droplet at new location

Greek symbols

σ : surface tension (N/m)
ζ : random value in range (-1,1)
μ_g: molecular viscosity of vapor (Pa·s)
μ_l: molecular viscosity of liquid droplet (Pa·s)
ρ_g : vapor density(kg/m^3)
ρ_d: droplet density (kg/m^3)
η_b: amplitude ratio between induced oscillation of a droplet and oscillation of the surrounding fluid eddy at the boundary edge
τ_+: dimensionless particle relaxation time, $\tau_+ = \left(\frac{u^{*2}\rho_g}{\mu_g}\frac{d_p^2\rho_d}{18\mu_g}\right)$

categorised as three-step model. During the calculation of wall-droplet heat transfer, it requires the droplet deposition velocity to account the droplet deposition flux. In previous three-step post-dryout mechanistic models, correlations for droplet deposition were derived from studies on the deposition process of metal or glass particles, as well as droplets in the annular flow regime on unheated surfaces. For example, the deposition in the mechanistic models [8–10] was calculated by correlations from solid particles deposition studies [11–13]. In their experimental studies, there is no heating from the surface and the wall surface is designed as sticky surface so that the particles will not rebound or re-suspend to the vapor flow as long as they deposit on the wall. Moreover, there are post-dryout models [14,15] calculated the droplet deposition according to the deposition correlations [16,17] developed from droplet deposition in annular flow [18–20]. Droplet deposition in dispersed flow has primarily been theoretically investigated, with very limited experimental work available. For example, in the experimental work of Mastanaiah and Ganic [21], an experimental study of droplet deposition in dispersed flow is conducted with non-heated wall. By collecting the liquid film flow generated by droplet deposition, the droplet deposition rate can be obtained. A correlation of droplet deposition derived in Ganic and Mastanaiah [22] is based the droplet diffusion equation considering that the droplet deposition is driven by the droplet concentration gradient between the tube center and the edge of the buffer layer. Similar correlations were developed in the works of Yang and Lee [23] and Matida and Torii [24] and used in the prediction of wall temperature in post-dryout region [25,26]. In these deposition correlations, the model from Beal [27] is utilized for the calculation of deposition mass flux at the edge of the buffer layer, which requires the value of droplet's sticking probability. But this sticking probability is always assumed to be unity in their works, which means that all droplets passing through the buffer layer are considered to stay there. The droplet rebounding is not considered in their models.

The experimental investigation on wall-droplet impact in Köhler and Hein [28] shows that the droplet cannot wet the wall with very high superheating. The experimental work of Kendall and Rohsenow [29] also found that the wall-droplet heat transfer effectiveness reduces ten times when the wall superheating over a certain value. Therefore, given the high wall temperature in the post-dryout region, there are some two-step models for post-dryout heat transfer ignoring the wall-droplet contact heat transfer [30–32]. And from the simulation result of Xia et al. [33], droplet evaporation on the wall accounts for less 2 % of the total evaporation. Half of the evaporation occurs within 1 mm from the wall due to the high vapor temperature in the near wall region. The droplets that migrate from the center of the tube, characterized by low vapor temperatures, toward the near-wall region with higher vapor temperatures influence the overall interfacial heat transfer. Consequently, the droplet transversely movement is not only important for wall-droplet heat transfer calculation, but also has great significance of the interfacial heat transfer. Considering the significance of interfacial heat transfer to the wall cooling in post-dryout region, the droplet lateral movement between high evaporation and low evaporation regions should be well investigated.

The experimental data of particle deposition velocity collected in McCoy and Hanratty [34] demonstrated a strong dependence on particle relaxation time, which is proportional to particle size and density. In the low relaxation time region, numerous experimental data points indicate that deposition velocity increases linearly with relaxation time. However, as relaxation time exceeds 23, this trend reverses, resulting in a negative slope in the deposition rate. When the relaxation time exceed 10^3, there are very few experimental data points available, but a decreasing trend continues as relaxation time increases. In the post-dryout region, droplets typically fall within a relaxation time range greater than 10^2,which is considered as a constant deposition rate of 0.17 [3]. The droplet size effect on the droplet deposition behavior in the

post-dryout region considering the droplet rebounding and droplet evaporation is still deficient. And the droplet evaporation and rebounding makes it very hard to obtaining droplet deposition parameters via experiment measurement. Therefore, to understand droplet deposition behavior in the post-dryout region, computational fluid dynamics (CFD) is an effective approach. In previous CFD simulations, solid particles deposition on the non-heated wall using the discrete particle method [35–38] were analysed, where the wall boundary condition is set as a trap boundary for discrete phase. Whenever the droplet touches the wall, it will be counted as trapped and removed from the flow region. Aguinaga et al. [39] simulated droplet deposition on an unheated surface including the droplet rebound, but without evaporation. Therefore, there is still big deficiency in CFD studies on droplet deposition behavior on heated surface with evaporation.

In this paper, the transverse movement of droplets in superheated turbulent vapor flow is studied with CFD simulation. The trajectories of single droplets and statistical character of radial velocity of droplets are showed. In light of the importance of droplet distribution on interfacial heat transfer, the droplet transverse mass flux and transverse velocity from the central region to the near-wall region, as well as the impact of evaporation on droplet deposition are also investigated in detail. The effect of droplet size on deposition with rebound and evaporation has also been carefully studied. This work delivers valuable insights for understanding and modelling droplet deposition behavior, contributing to the development of mechanistic models for post-dryout heat transfer.

2. Computational model

The current simulation has been carried out using the CFD code ANSYS Fluent [40], which offers a wide range of multiphase flow models. Among them, the discrete particle model (DPM) is selected for the investigation on droplet behaviors in post-dryout region. In DPM method, the continuous phase is solved in Eulerian meshes, while the dispersion phase is tracked in Lagrangian coordinates. The droplet trajectories are computed by integrating the force balance individually at specified intervals during the fluid phase calculation. The droplets exchange momentum, mass, and energy with the vapor phase when the droplets passing through a vapor control volume. The turbulence interaction between the two phases is treated as one-way coupling, meaning that only the turbulence in the vapor phase influences droplet motion, while the droplets' motion is assumed not to impact the turbulence characteristics of the vapor phase. With this method, the droplet trajectory and thermal parameters can be obtained easily. The grid size can be relative larger than the droplet size since the droplets are tracked separately in Lagrangian coordinates. Besides, the DPM calculation only needs to solve the conservation equations for continuous phase and droplet motion equation. The interaction between phases is included in the source term of conservation equations. Therefore, the calculation efficiency with the DPM method is quite high compared to other multi-phase methods such as volume of fluid method (VOF) and Eulerian-Eulerian method. However, this method can only be suitable for dispersion flow with low droplet volume fraction because it ignores the interaction between droplets and the existence of droplet volume in Eulerian mesh. In the post-dryout region, a vapor mass fraction of >80 % is taken. Usually. the vapor volume fraction is much larger than 90 % and the negligence of the interaction between droplets is thus reasonable. Therefore, the application of the Discrete Phase Model (DPM) in the present study is feasible and of advantages.

During the simulation, the vapor flow is treated as the continuous phase and is solved in Eulerian meshes. The *k-epsilon* turbulence model is selected for the calculation of turbulence parameters of vapor flow. The enhanced wall treatment is added to introduce a two-layer near-wall model to predict the vapor flow and droplet behaviors more precisely in the near-wall region. The enhanced wall function necessitates a fine mesh in the near wall and requires the y^+ value <1. The meshes in the vicinity of the wall are more refined accordingly and making sure that all the mesh in the first layer keep the y^+ value <1. In this case, the meshed in the first layer is smaller than the droplet size. But the mesh size primarily affects the calculation accuracy of the continuous phase, while the tracking of droplets is independent of the Eulerian phase mesh. The mesh sensitivity has been done and reported in Xia et al. [33]. The vapor properties, such as density, heat capacity, etc. are given in dependence on temperature and pressure.

2.1. Droplet motion and interfacial interaction

The droplet trajectory in Lagrangian coordinates is controlled by the Eq. (1) in ANSYS Fluent [40]:

$$m_d\frac{d\vec{u}_d}{dt}=m_d\frac{\vec{u}_g-\vec{u}_d}{\tau_r}+m_d\frac{\vec{g}(\rho_d-\rho_g)}{\rho_d}+\vec{F} \tag{1}$$

where m_p is the droplet mass, $\vec{u}_p$ the droplet velocity, $\vec{u}_g$ the vapor velocity. $\vec{F}$ the additional force. In this simulation, incorporating extra forces, such as lift force, would result in a substantial computational burden without enhancing the accuracy of wall temperature predictions. Furthermore, these forces rely on empirical models, which introduce uncertainties and complicate the analysis of droplet behaviors with evaporation. Therefore, only the interfacial drag force is considered in this study. The first item on the right-hand side is the drag force, and τ_r is the droplet relaxation time and calculated by Eq. (2):

$$\tau_r=\frac{\rho_d d_p^2}{18\mu_g}\frac{24}{C_D Re_d} \tag{2}$$

The relative Reynolds number Re_d is calculated with:

$$Re_d=\frac{\rho_g d_p\left|\vec{u}_g-\vec{u}_d\right|}{\mu_g} \tag{3}$$

In this paper the spherical drag law is considered to calculate the drag coefficient:

$$C_D=a_1+\frac{a_2}{Re_d}+\frac{a_3}{Re_d^2} \tag{4}$$

a_1, a_2, a_3 are constants and given by Morsi and Alexander [41].

The stochastic tracking model is used to predict the dispersion of particles caused by the turbulence of vapor phase. The vapor velocity used in Eq. (1) is calculated by Equations (5) - (7). This method includes the impact of instantaneous turbulent velocity fluctuations on the droplet trajectories. Taking the velocity component in x coordinate (u) as an example:

$$u_g=\overline{u}_g+u' \tag{5}$$

$$u'=\zeta\sqrt{\overline{u'^2}} \tag{6}$$

Where u' is the vapor fluctuation velocity, ζ a normally distributed random number, $\sqrt{\overline{)u'^2}}$ the local root mean square (RMS) of vapor velocity fluctuation, which is considered isotropic and determined by the turbulent kinetic energy k:

$$\sqrt{\overline{u'^2}}=\sqrt{\overline{v'^2}}=\sqrt{\overline{w'^2}}=\sqrt{2k/3} \tag{7}$$

With known the droplet velocity, the droplet trajectory is predicted by:

$$\frac{dx_d}{dt}=u_d \tag{8}$$

The new position of the droplet is computed by a trapezoidal discretization:

$$x_d^{n+1} = x_d^n + \frac{1}{2}\Delta t\left(u_d^{n+1} + u_d^n\right) \tag{9}$$

2.2. Interfacial energy, mass and momentum exchange

During the computation of droplet trajectories, the change of their heat, mass, and momentum are also calculated. Fig. 1 shows the interaction between phases when one droplet passes an Eulerian mesh. After the exchange of mass, energy and momentum with vapor phase, the parameters of droplets, like velocity, size and trajectory as well as the parameters of vapor will change. These exchanges are then incorporated into subsequent calculation for the continuous vapor phase. This two-way coupling is achieved by alternately solving the discrete and continuous phase equations until the solutions for both phases converge.

2.2.1. Interfacial momentum exchange

When the droplets pass through the control volume of the vapor phase, the droplets can be accelerated or decelerated under the effect of drag force between phases. During this process, there will be momentum transfer between the continuous phase and the discrete phase. The CFD model examines the change in momentum of every droplet and sums all the momentum change to the momentum source of the momentum equation of the continuous phase:

$$F_M = \sum\left(\frac{18\mu C_D Re_d}{\rho_d d_p^2 24}\left(u_d - u_g\right)\right)G_d\Delta t \tag{10}$$

2.2.2. Interfacial heat and mass transfer

The heat transfer between droplet and vapor in current simulation is calculated by:

$$Nu_{v-d} = \left(2 + 0.6Re_d^{\frac{1}{2}}Pr^{\frac{1}{3}}\right)\log_e\left[1 + \frac{c_{p,g}\left(T_g - T_d\right)}{h_{lg}}\right] \tag{11}$$

The mass and heat transfer between the droplets and the vapor phase are calculated by counting the mass and energy change of all the droplets as they pass through one control volume. The calculated mass and energy exchange is represented as the source term in the continuity and energy equation of the continuous phase.

$$M = \frac{m_{d,in} - m_{d,out}}{m_{d,0}}G_{d,0} \tag{12}$$

$$Q = \frac{G_{d,0}}{m_{d,0}}\left[-\left(m_{d,in} - m_{d,out}\right)h_{lg} + m_{d,in}c_{p,d}\Delta T_{d,in} - m_{d,out}c_{p,d}\Delta T_{d,out}\right] \tag{13}$$

2.3. Droplet wall interaction model

When a droplet moves to the boundary cell, it has a possibility to impinge on the wall. During the impingement, the droplet deforms into a cylinder and remains in direct contact with the heated wall for a short period of time (contact time) before rebounding. During the contact time, the droplets get heat from the heated wall and later are rebounded back to the flow. The heat transfer from the wall to the droplet is calculated as following equations:

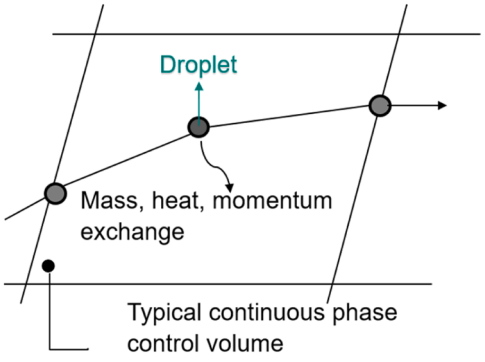

Fig. 1. . Schematic of interfacial interaction(ANSYS Fluent [40]).

$$m_d c_{p,d} T_d = \int_0^{t_d} \frac{k_l A_{cont}}{H_{wd}}\left(T_w - T_d\right)dt \tag{14}$$

The A_{cont} is the contact area between the deformed droplet and wall, calculated according to Akao et al. [42]:

$$A_{cont} = \frac{\pi D_{max}^2}{8} \tag{15}$$

$$D_{max} = 0.61 D_0 We^{0.38} \tag{16}$$

The contact time t_d is calculated according to Birkhold [42,43]:

$$t_d = f\frac{\pi}{4}\sqrt{\frac{\rho_d D_0^3}{\sigma}} \tag{17}$$

2.4. Boundary conditions

The test section used for the investigation on droplet behavior in post-dryout region is shown in Fig. 2. The experimental case of No.276 from Becker et al. [44] is selected as the reference condition and summarized in Table 1. At this case the steam quality at dryout point is very high and the volume fraction of droplets is <1 %, which perfectly meets the requirements of using DPM model and ensures minimal errors in the calculation of vapor velocity in Eulerian mesh. Additionally, 7 MPa is a common operating pressure in thermal power plant, nuclear power plant, and some industrial heat exchange systems, especially in applications involving efficient heat exchange and cooling. From the droplet size model of Ueda and Kim [45], the calculated average droplet size under this condition is approximately 0.1 mm. To assess the influence of droplet size on droplet lateral movement, three initial diameters of the droplet d_{p0}, i.e. 0.05 mm, 0.1 mm and 0.2 mm are selected.

2.5. Model validation

Fig. 3 presents the predicted wall temperatures of the reference cases compared with experimental data. The predicted wall temperatures with three initial droplet sizes encompass the profile of the measured wall temperatures from the experiment. This agreement demonstrates the reliability of the current CFD model for simulating post-dryout heat transfer. It is also observed that injecting smaller droplets results in lower predicted wall temperatures, highlighting the significant influence of droplet size on post-dryout heat transfer. More information about the model validation can be found in Xia et al. [33].

3. Results and discussion

The calculated droplet evaporation rates are detailed analysed in Xia et al. [33]. This paper focuses on the analysis of droplet lateral movement and deposition behaviors. In this section, the trajectory of a single droplet is presented to illustrate its transverse movement in the post-dryout region. Given that droplet motion is influenced by random fluctuations in velocity, the radial velocities of droplets are displayed in histogram form to statistically represent their radial movements. The average radial velocity of droplets toward the wall is plotted against radial distance to examine how the group's radial velocity changes as they approach the wall. Additionally, as it showed that droplet evaporation rate density in the central region differs greatly from that in the near-wall region (Xia et al. 2024), three deposition parameters, net deposition mass flux, deposition velocity and entrainment velocity are introduced to quantitatively assess the mass flux and velocity of droplet

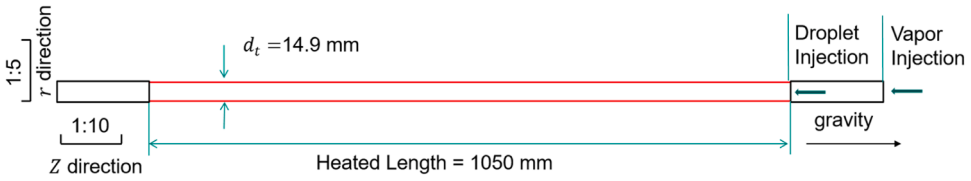

Fig. 2. Geometry of the circular tube for CFD simulation.

Table 1
Boundary conditions of reference cases.

	Pressure [MPa]	Mass Flux [kg/(m^{2}s)]	Heat Flux [kW/m^2]	Dryout quality	Droplet diameter [mm]
Reference Case1	7.0	500	466	0.883	0.1
Reference Case2	7.0	500	466	0.883	0.2
Reference Case3	7.0	500	466	0.883	0.05

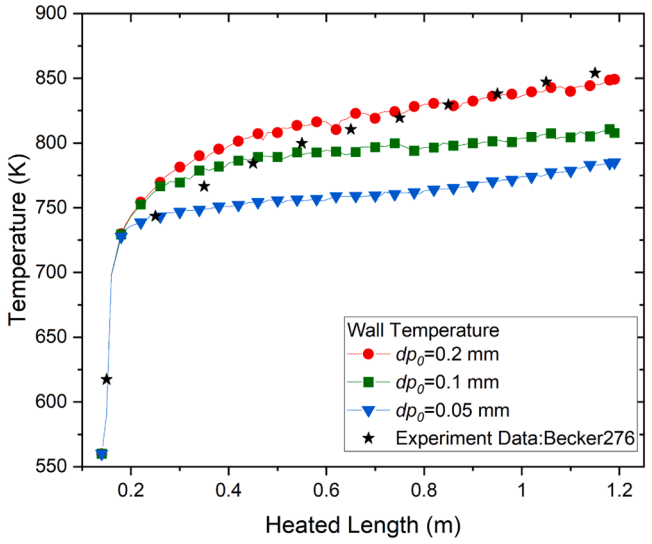

Fig. 3. Comparison of experimental and predicted wall temperature (Xia et al. [33]).

exchange between the central region and the near-wall region. The impacts of droplet size and evaporation on droplet deposition behaviors are detailed showed and analysed based on these three parameters.

3.1. Droplet trajectory

From the Equations (1), the droplets lateral movement in the vapor flow is under the effect of drag force, which is calculated by the velocity difference of instantaneous vapor velocity and droplet velocity. From the stochastic dispersion method, the instantaneous vapor velocity is calculated by the time-averaged velocity plus the fluctuation velocity, as presented in Eq. (5). In the radial direction, the time-averaged velocity is very small compared with the fluctuation velocity. The droplet transverse movement in vapor flow is mainly controlled by the fluctuation velocity. Here the trajectories of four droplets (with number 1, 2, 3 and 4) with initial diameter $d_{p0} = 0.2$mm are shown in Fig. 4. Their trajectories are tracked in 25 time steps with time step length 0.001 s. The x-axis is the droplet position in the z-direction and the y-axis is the droplet position in the radial direction from the droplet to the center of the tube. The red arrow represents the radial velocity of the droplet at the current position, with its length indicating the velocity magnitude and its direction corresponding to the direction of motion. When the arrowheads direct toward the decrease of the radial position, the radial velocity is negative, indicating that the droplet is moving away from the heated wall.

Fig. 4(a) shows a routine of droplets leaving the near wall region. During the lateral movement, the droplet also moves from a height of 0.65 m to 1.0 m in axial direction. Initially, the droplet fluctuates in the near-wall region, where its radial velocity is so small that the arrow is nearly invisible. As it moves away from the wall, its radial velocity increases. This rise in velocity generates a larger interfacial drag force, causing the velocity to decrease until the droplet reaches a radial distance of 6.6 mm. Afterward, the droplet accelerates again by the fluctuation velocity and moves to the tube center in a relative high speed. The droplet trajectory in Fig. 4(b) illustrates the trajectory of a droplet moving towards the wall, encountering a more tortuous path. Initially, the droplet attempts to approach the wall, but experiences a deceleration and is even temporarily directed in the opposite direction. Subsequently, it can be inferred that it passes the control volumes with fluctuation velocity towards the wall, which enables it to resume its movement towards the wall. After several time steps of gradually approaching the wall, it can be expected that there is a high probability that the droplet eventually reaches the wall in next time steps. Fig. 4(c) shows the trajectory of a droplet who has reached the wall and impacted with the wall. The droplet initially fluctuates at the edge of near wall region. Then it accelerates approaching the wall and finally touch the wall in a large velocity. The impaction with the wall rebound the droplet back to the flow with a direction change in velocity. After the reflection the droplet moves toward the main flow with a decreasing velocity. In contrast, Fig. 4(d) shows a droplet attempting to approach the wall but continuously decelerating in the process. Its velocity becomes nearly imperceptible as it reaches the region very close to the wall. The droplet fluctuates in the close wall region until the last three time steps. It acquires a small negative radial velocity but still remains in the near-wall region. The comparison of trajectories between droplet No 3 and No.4 reveals that droplets exhibit different behaviors when moving toward the wall: some droplets can be accelerated and eventually reach the wall and bounce back, while others might be decelerated, reach a position very close to the wall and fluctuate in the near-wall region.

These trajectories suggest that the droplets suffer randomly drag force in direction and amount due to the randomness of turbulence. Only those, that regain sufficient radial velocity through turbulent exchange with vapor phase, can eventually reach the wall. Moreover, droplets passing through the buffer layer may either be reflected back into the main flow, become trapped within the buffer layer, or fluctuate within the near-wall region.

3.2. Droplet radial velocity

To statistically analyze droplet lateral movement, the distribution and average droplets radial velocity are selected as key parameters of interest from the simulation results. To ensure statistical significance by selecting an adequate number of droplets, a target volume with a height of Δz and a thickness of d_r are chosen at a radial distance of r_c from the center of the tube. d_r is defined as 0.1 times the distance to the wall. All

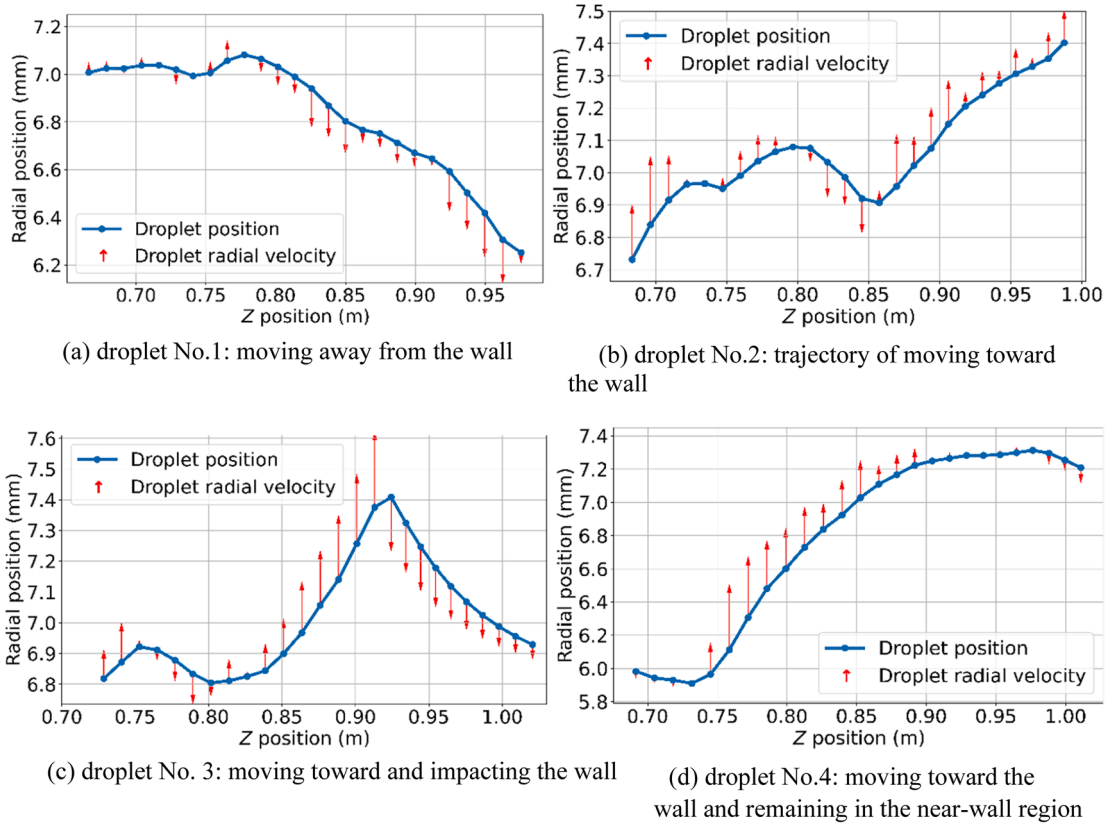

(a) droplet No.1: moving away from the wall

(b) droplet No.2: trajectory of moving toward the wall

(c) droplet No. 3: moving toward and impacting the wall

(d) droplet No.4: moving toward the wall and remaining in the near-wall region

Fig. 4. Examples of droplet trajectory and changes in droplet radial velocity along the trajectory at reference case 2 of $d_{p0} = 0.2$ **mm**.

the droplets in this volume are collected. To investigate the droplet lateral movement, the droplets radial velocities are presented as a histogram, displaying the value of droplet radial velocity and the corresponding droplet count in this velocity range. The radial distance of r_c is set to 7 mm as an example to display the droplets radial velocities distribution in the near wall region, as this is the point where both vapor temperature and evaporation rate density begin to increase[33]. The Δz is set to 0.3 m to ensure a sufficient number of droplets are collected for analysis. For instance, in the case with $d_{p0} = 0.2$ *mm*, although the mass flux is the same as in other cases, the larger droplet diameter results in a lower total amount of droplets. Nevertheless, approximately 6000 droplets can still be collected within the target volume.

In Fig. 5 and Fig. 6, the radial velocity of droplets in the cases of $d_{p0} = 0.2$mm and $d_{p0} = 0.05$mm are selected to illustrate the distribution of droplet radial velocity and to examine the effect of droplet size. The width of each bin is 0.02 m/s.

As can be seen from Fig. 5(a) and Fig. 6(a), the distribution of droplets with positive radial velocity roughly conforms to the normal distribution in positive *x*-axis. However, Fig. 5(b) reveals an anomalously high concentration of droplets with small negative radial velocities, a trend that becomes even more pronounced in Fig. 6(b). Approximately 2000 out of 6000 droplets (33 %) in case of $d_{p0} = 0.2$mm have very small negative radial velocity. In the case of $d_{p0} = 0.05$ mm, 35,000 out of 40,000 droplets fall into this category, accounting for as high as 87.5 %. These figures indicate that smaller droplet sizes are associated with a higher proportion of droplets exhibiting small negative radial velocities. Additionally, droplets with smaller initial droplet sizes display a broader range of radial velocities in both directions. However,

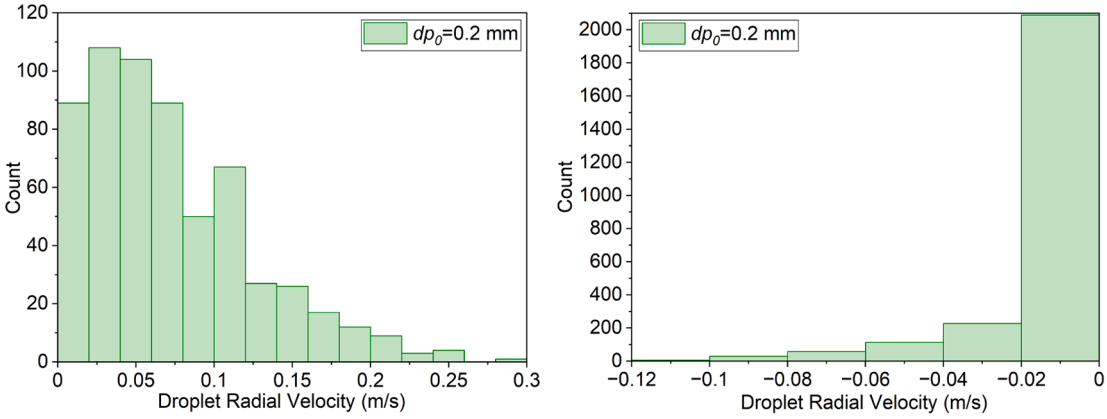

(a) Droplets with positive radial velocity

(b) Droplets with negative radial velocity

Fig. 5. Histogram of droplet radial velocities of reference case 2 with $d_{p0} = 0.2$ **mm**.

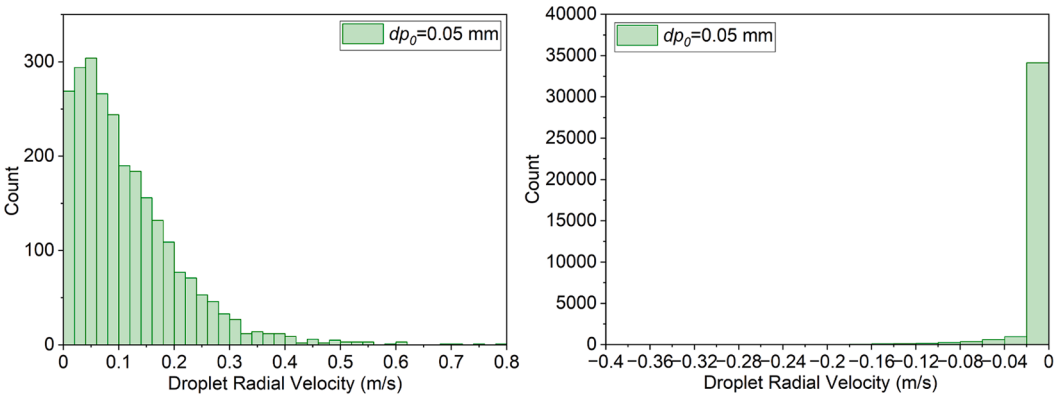

(a) Droplets with positive radial velocity (b) Droplets with negative radial velocity

Fig. 6. . Histogram of droplet radial velocities of reference case 3 with $\boldsymbol{d_{p0}}$ = 0.05 **mm**.

droplets with large radial velocities are relatively rare, for instance, in the case with d_{p0} = 0.2mm, only 42 droplets have radial velocities exceeding 0.4 m/s, comprising just 1.65 % of all droplets with positive radial velocities. Similarly, only 5 droplets exhibit radial velocities smaller than −0.4 m/s. Comparing the number of droplets with absolute radial velocities greater than 0.1 m/s, there are 2424 droplets in the left-hand figure and only 487 droplets in the right-hand figure. The averaged droplet radial velocity with positive values is called average deposition velocity in the following text. In the case with d_{p0} = 0.2mm the average deposition velocity is 0.111 m/s, while in the case with d_{p0} = 0.05mm it is 0.205 m/s.

From the droplet trajectory showed in Fig. 4, the droplet radial velocity always changes when it approaches the wall. Thus, by adjusting the value of r_c, droplets are collected at varying distances from the wall to observe the radial profile of the average droplet deposition velocity. In Fig. 7, the *x*-axis is the distance from the collection region to the tube center r_c divided by the tube radius *R*. The *y*-axis is the average deposition velocity at this radial position. The error bars in the figure is the standard error (SE) of droplet average deposition velocity. The deposition velocity profile exhibits a decreasing trend as the distance to the wall decreases. A significant difference in deposition velocity is observed between the central region and the near-wall region. The deposition velocity for droplets with smaller initial sizes is consistently higher than for those with larger initial sizes. Therefore, the droplet diameter has a pronounced effect on the droplet deposition velocity.

The presence of numerous droplets with small negative velocities makes analyzing the droplets moving toward the center statistically insignificant. To more effectively capture the overall lateral movement of the droplets, three deposition parameters, droplet deposition mass flux, deposition velocity and entrainment velocity are derived based on the method illustrated in Fig. 8. At time *t*, a target volume with a height of Δz^0 is selected, and the flow domain is divided into a central region and a near-wall region based on a cutoff distance r_c. For the subsequent analysis, r_c is set to 7 mm as the previous analysis. Sensitivity analysis is also performed with different values of r_c and found that the selection of r_c value doesn't affect the trends of deposition parameters in the near wall region. After one time step Δt, the height of the target volume is extended to Δz^1. The distance of Δz^1 is based on the criterion that the axial distance traveled by droplets within one time step cannot exceed the length difference $\Delta z^1 - \Delta z^0$. At time $t + \Delta t$, droplets are identified again and compared with the droplets collected at the previous time point. Droplets that were in the central region at time *t* and appear in the near-wall region at time $t + \Delta t$ are identified as depositing from the central region to the near-wall region. Similarly, droplets that were in the near-wall region at time *t* but are found in the central region at time $t + \Delta t$ are classified as entrained from the near-wall region to the central region. The corresponding mass flux is calculated by:

$$\dot{m}_{d,c-n} = \frac{\sum_0^i m_{d,c-n}}{\Delta t * \Delta z^0 * 2r_c * \pi} \tag{18}$$

$$\dot{m}_{d,n-c} = \frac{\sum_0^j m_{d,n-c}}{\Delta t * \Delta z^0 * 2r_c * \pi} \tag{19}$$

$$\dot{m}_{d,net} = \frac{\sum_0^i m_{d,c-n} - \sum_0^j m_{d,n-c}}{\Delta t * \Delta z^0 * 2r_c * \pi} \tag{20}$$

Where the $\dot{m}_{d,c-n}$, $\dot{m}_{d,n-c}$ and $\dot{m}_{d,net}$ are the droplet mass flux from central region to the near-wall region, droplet mass flux from near-wall region to the central region, and the net mass flux of droplets moving from central region to the near wall region. The calculated mass fluxes of reference cases 1–3 are shown in Table 2. It is evident that, in contrast to

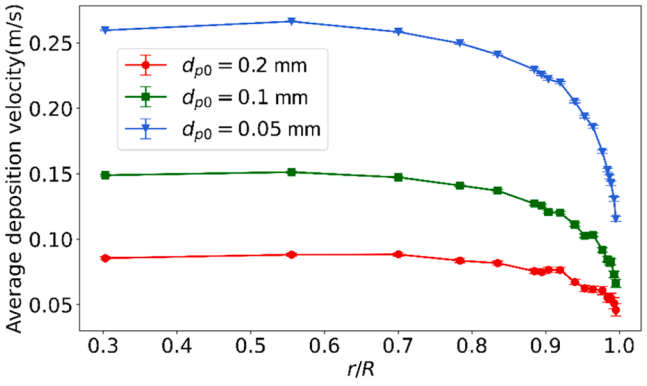

Fig. 7. Radial distribution of average droplet deposition velocity with different droplet size.

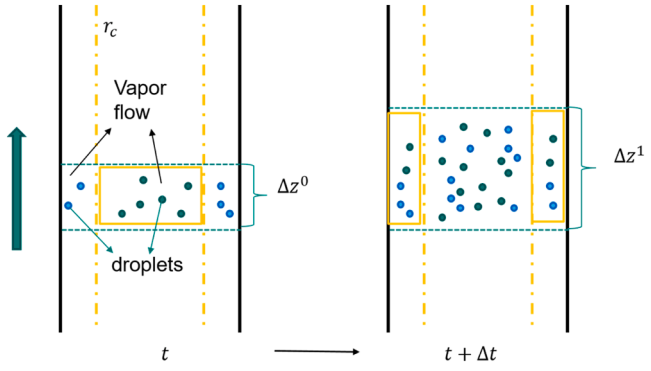

Fig. 8. Schematic of method for the derivation of deposition parameters.

Table 2
Droplet deposition mass flux of reference cases.

	$\dot{m}_{d,c-n}$	$\dot{m}_{d,n-c}$	$\dot{m}_{d,net}$
	[kg/(m^2 · s)]	[kg/(m^2 · s)]	[kg/(m^2 · s)]
d_{p0} = 0.05 mm	0.06498	0.02079	0.04419
d_{p0} = 0.1 mm	0.07937	0.03149	0.04788
d_{p0} = 0.2 mm	0.09328	0.04996	0.04332

the results presented in Fig. 7 —where smaller droplets exhibit higher average deposition velocities—the droplet mass flux from the central region to the near-wall region, as shown in Table 2 increases with droplet size. However, as the droplet mass flux from the near-wall region back to the central region also increases with droplet size, the net deposition flux does not show a clear dependence on droplet size.

In cases with different initial droplet sizes, varying droplet mass concentrations are observed along the same heating length due to differences in evaporation rates. Larger droplets, with lower evaporation rates, retain higher mass concentrations, which in turn influences droplet deposition. Therefore, to eliminate the influence of droplet concentration, the droplet lateral movement velocity is calculated by:

$$k_{d,c-n} = \frac{\dot{m}_{d,c-n}}{C_{d,c}} \tag{21}$$

$$k_{d,n-c} = \frac{\dot{m}_{d,n-c}}{C_{d,n}} \tag{22}$$

$C_{d,c}$ and $C_{d,n}$ are the droplet mass concentration in the central region and in the near-wall region. The derived droplet lateral velocities $k_{d,n-c}$ and $k_{d,c-n}$ are referred to as deposition velocity and entrainment velocity in this study, representing the lateral exchange velocity of droplets between two regions. The calculated results are displayed in Table 3 and show that after removing the influence of droplet concentration, the deposition velocity of droplets from the central region to the near-wall region increases as droplet size decreases, which is consistent with the conclusion in Fig. 7. The cases with smaller droplet sizes also exhibit greater velocities from the near-wall region to the central region. For instance, the entrainment velocity of the case with d_{p0} = 0.05mm is twice that of case with d_{p0} = 0.1mm. This comparison highlights the dependence of droplet deposition velocity on droplet size.

Previous deposition correlations typically estimate deposition velocities by calculating the rate at which particles deposit from the turbulent core to the edge of the buffer layer, corresponding to a y^+ value of approximately 30. For comparison with correlations in the literature, the boundary between the central and near-wall regions is now set at y^+= 30, where the value of r_c is 6e-5, as derived from the CFD-calculated wall shear stress. The deposition mass flux between the turbulent core and the buffer layer is calculated and shown in Table 4. The calculated deposition and entrainment mass fluxes at y^+= 30 are significantly smaller than those in Table 2, consistent with the trend in Fig. 7, where droplet deposition velocity decreases as particles approach the wall. The correlations of Yang[23], Friedlander[11] and Kataoka [16] are displayed in Table 5. The calculated deposition velocity obtained from the simulation and literature are compared Table 6. It shows that the deposition velocity of correlations from literature are much larger than the CFD simulation results. Considering the droplet entrainment, the net droplet deposition mass flux is less in the CFD simulation. This comparison further proves the idea that the current droplet deposition models are not suitable for the post-dryout heat transfer.

Table 3
Droplet deposition velocity and entrainment velocity of reference cases.

	$k_{d,c\text{-}n}$ [m/s]	$k_{d,n\text{-}c}$ [m/s]
d_{p0} = 0.05 mm	0.05182	0.01971
d_{p0} = 0.1 mm	0.03937	0.00664
d_{p0} = 0.2 mm	0.03146	0.00893

Table 4
Droplet deposition mass flux from turbulent core to buffer layer of reference case 1.

	$\dot{m}_{d,c-n}$ [kg/(m^2 · s)]	$\dot{m}_{d,n-c}$ [kg/(m^2 · s)]	$\dot{m}_{d,net}$ [kg/(m^2 · s)]
d_{p0} = 0.1 mm	0.05119	0.04457	0.00662

Table 5
Droplet deposition correlations from literature for comparison.

Authors	Correlations
Yang and Lee [23]	$k_d = u^* \dfrac{1.224\eta_b}{1.33 + 2.44\eta_b ln\left(\dfrac{1+2\left(1-30/Re\sqrt{C_f/2}\right)^2}{1-\left(1-30/Re\sqrt{C_f/2}\right)^2}\right)}$
Friedlander and Johnstone [11]	$k_d =$ $u^* \dfrac{1}{\dfrac{1}{\sqrt{C_f/2}} + \left(\dfrac{1525}{0.81\tau_+^2} - 50.6\right)}$ $\tau_+ < 5.6$
	$u^* \dfrac{1}{\dfrac{1}{\sqrt{C_f/2}} - 13.73 + 5\, ln\left(\dfrac{5.04}{\tau_+} - 0.959\right)}$ $5.6 \le \tau_+ < 33.3$
	$u^*\sqrt{C_f/2}$ $\tau_+ \ge 33.3$
Kataoka et al. [16].	$k_d = \dfrac{\mu_g}{d_t} 0.22 Re_l^{0.75} \left(\dfrac{\mu_g}{\mu_l}\right)^{0.26}$

Table 6
Comparison of deposition velocities from turbulent core to buffer layer across different models

	$k_{d,c\text{-}n}$ in Current Simulation	Yang Correlation [23]	Friedlander Correlation [11]	Kataoka Correlation [16]
Deposition Velocity (m/s)	0.02198	0.14280	0.04313	0.53519

3.3. Evaporation effect on droplet deposition

In the post-dryout region, droplet evaporation alters the profiles of vapor temperature and velocity, which in turn influence droplet behavior, as also noted by Meholic [10]. Given the more intense evaporation near the wall, it can be inferred that the impact of evaporation on droplet trajectories is likely more pronounced in this region. However, the effects of evaporation on droplet deposition have not been extensively investigated, and experimental studies are particularly challenging. CFD simulations, by contrast, offer valuable insights into droplet deposition behavior under evaporative conditions. This subsection will thoroughly examine and analyze the effect of droplet evaporation on the droplet movement between the central region and near-wall region.

3.3.1. Calculation method

To study the effect of evaporation on droplet deposition, the models for interfacial heat and mass transfer in the case without evaporation are modified as follows: droplets absorb heat from the superheated vapor, but will not evaporate and no mass transfer between phases takes place. Numerical simulations for both cases—with and without evaporation—are conducted under the same constant wall temperature to ensure more comparable vapor temperature profiles than would be achieved using a constant wall heat flux. Apart from the wall boundary condition, the initial conditions follow those outlined in Table 1. A

constant wall temperature of T_w=800 K is applied, as this value closely matches the average measured wall temperature.

3.3.2. *Evaporation effect on droplets radial velocity*

Fig. 9 presents the histogram of droplet radial velocities for the case with evaporation, which aligns with the trend observed in Fig. 6: the droplets with positive radial velocity in Fig. 9(a) almost follow the normal distribution in positive half-axis, while a considerable number of droplets have a smaller negative radial velocity in Fig. 9(b). Fig. 10 shows the histogram of droplet radial velocities in the case without evaporation. The droplets with positive radial velocity in Fig. 10(a) do not follow a Gaussian distribution, with a greater number of droplets with smaller positive radial velocity. Additionally, Fig. 10(b) indicates a reduction in the number of droplets with small negative radial velocities compared to the case with evaporation shown in Fig. 9(b). This comparison suggests that, in the presence of evaporation, more droplets tend to move away from the wall rather than towards it. Evaporation significantly impacts the radial velocities of the droplets, particularly by altering the direction of droplets with small positive radial velocities, thereby reducing the number of droplets moving towards the wall.

The substantial increase in the number of droplets with small positive radial velocities renders the average velocity an inadequate metric for representing the statistical characteristics of droplet radial velocity in cases without evaporation. To analyze the effect of evaporation on the droplet deposition behaviors, the net deposition mass flux, deposition velocity and entrainment velocity, defined in Eq.(18) – (22), are displayed in Table 7 and Table 8 with constant wall temperature of 800 K but different initial droplet size. The column of net deposition mass fluxes for different droplet sizes in the Table 7 reveals that, in the absence of evaporation, the net deposition mass flux decreases significantly as droplet size increases. This trend is not observed under conditions with evaporation, as shown in Table 8. Additionally, the data indicates that smaller droplets have a higher net deposition mass flux. The net deposition mass flux increases nearly fivefold when the injected droplet size reduced from 0.2 mm to 0.1 mm. The increase in net deposition mass flux is less pronounced when the size decreases further from 0.1 mm to 0.05 mm.

The deposition velocity and entrainment velocity represent the lateral movement of droplets, independent of droplet mass concentration. In the absence of evaporation, the 2 times increase in the droplet size brings an approximately 1.5 times reduction in the deposition velocity. With evaporation, the increase trend in deposition velocity with decreasing droplet size is less pronounced compared to the case without evaporation. In contrast, the entrainment velocity rises with increasing droplet size. As the size increases from 0.05 mm to 0.1 mm, the entrainment velocity with evaporation only increases slightly while in the case without evaporation it has nearly 3 times growth. From the comparison of three deposition parameters in Table 7 and Table 8, it can be concluded that cases with smaller droplets tend to have a larger deposition velocity but a smaller entrainment velocity. Evaporation will reduce the deposition velocity and increase the entrainment velocity.

To prove the above conclusion, further simulations are conducted with two different wall temperatures (600 K, 1000 K) and d_{p0} = 0.1mm. The three cases represent weak evaporation (600 K), medium evaporation (800 K) and strong evaporation (1000 K), respectively. Table 9 presents the total evaporation rate across the entire flow region for three different wall temperatures, illustrating varying evaporation intensities. As the wall temperature increases, the total evaporation rate also rises. Specifically, increasing the wall temperature from 600 K to 800 K results in a threefold increase in the evaporation rate.

In Table 10, the deposition parameters under the three wall temperatures with evaporation are displayed. With the increase of wall temperature, the net deposition mass flux decreases. The deposition velocity also decreases while the entrainment velocity increases. It can be observed that higher evaporation rates lead to a lower deposition rate and a higher entrainment rate. At higher wall temperatures, droplets are smaller at the same position. Previous analysis has shown that smaller droplets typically have higher deposition velocity. However, despite high evaporation rates, these smaller droplets still demonstrate lower deposition velocity. This indicates that evaporation has a more pronounced inhibition effect on deposition. Table 11 gives the deposition parameters at three different wall temperatures without evaporation. The results show that as the wall temperature increases, neither the deposition flux nor the deposition velocity exhibits significant change in cases without evaporation. Only the entrainment rate increases slightly with the rise in wall temperature, much weaker compared to the case with evaporation. When comparing the deposition velocities in both cases—with and without evaporation—it is clear that evaporation reduces the droplet deposition velocity while increasing the entrainment velocity. As the wall temperature increases, evaporation becomes more intense, leading to a more pronounced suppression effect on the deposition velocity. In contrast, evaporation has a more significant effect on enhancing the entrainment velocity, even at lower wall superheats where evaporation is less significant. As evaporation intensity rises, the entrainment velocity of droplets increases by approximately 2 to 3 times compared to conditions without evaporation. This comparison clearly indicates that evaporation not only inhibits droplet deposition but also significantly enhances droplet movement to the tube center. The more intense the evaporation, this evaporation effect on droplet deposition behaviors is more pronounced.

Therefore, the droplet deposition model developed from the unheated surface is not well suitable for the calculation of droplet deposition in post-dryout region. The correlations for droplet deposition with evaporation should be re-considered.

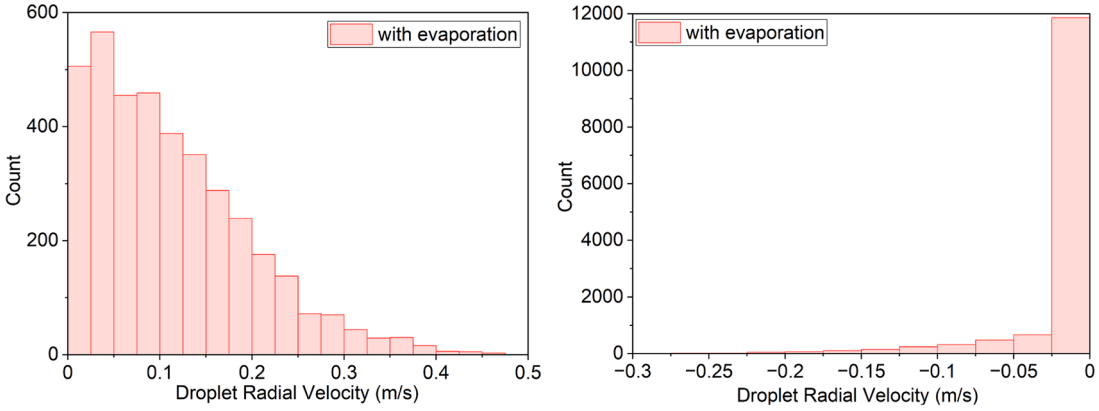

(a) Droplets with positive radial velocity (b) Droplets with negative radial velocity

Fig. 9. Histogram of droplet radial velocities for the case with Tw = 800 K and d_{p0}=0.1 mm, including droplet evaporation.

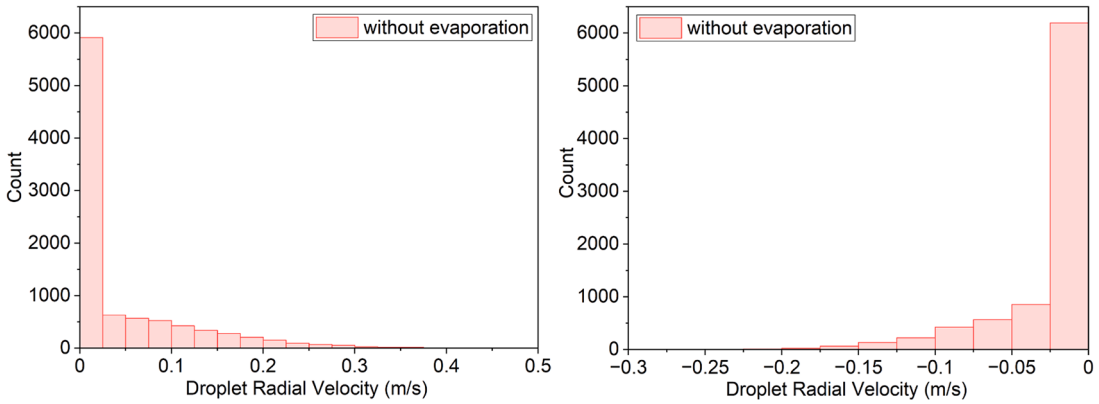

(a) Droplets with positive radial velocity (b) Droplets with negative radial velocity

Fig. 10. Histogram of droplet radial velocities for the case with Tw = 800 K and $\boldsymbol{d_{p0}}$=0.1 mm, excluding droplet evaporation.

Table 7
Droplet deposition parameters in the case of Tw = 800 K without evaporation.

	$\dot{m}_{d,net}$ [kg/(m^2 · s)]	$k_{d,c\text{-}n}$ [m/s]	$k_{d,n\text{-}c}$ [m/s]
d_{p0} = 0.05 mm	0.09497	0.06865	0.00272
d_{p0} = 0.1 mm	0.07600	0.04680	0.00351
d_{p0} = 0.2 mm	0.01691	0.02441	0.00812

Table 8
Droplet deposition parameters in the case of Tw = 800 K with evaporation.

	$\dot{m}_{d,net}$ [kg/(m^2 · s)]	$k_{d,c\text{-}n}$ [m/s]	$k_{d,n\text{-}c}$ [m/s]
d_{p0} = 0.05 mm	0.03481	0.04524	0.00267
d_{p0} = 0.1 mm	0.04842	0.04030	0.00721
d_{p0} = 0.2 mm	0.02685	0.02604	0.00925

Table 9
Evaporation rate in flow region.

	T_w = 600 K	T_w = 800 K	T_w = 1000 K
Total evaporation rate (kg/s)	0.001783	0.005371	0.006537

Table 10
Droplet deposition parameters for $\boldsymbol{d_{p0}}$=0.1 mm at different wall temperatures: with evaporation.

	$\dot{m}_{d,net}$ [kg/(m^2 · s)]	$k_{d,c\text{-}n}$ [m/s]	$k_{d,n\text{-}c}$ [m/s]
T_w = 600 K	0.06083	0.04140	0.00356
T_w = 800 K	0.04842	0.04030	0.00721
T_w = 1000 K	0.03121	0.02664	0.01245

Table 11
Droplet deposition parameters for $\boldsymbol{d_{p0}}$=0.1 mm at different wall temperatures: without evaporation.

	$\dot{m}_{d,net}$ [kg/(m^2 · s)]	$k_{d,c\text{-}n}$ [m/s]	$k_{d,n\text{-}c}$ [m/s]
T_w = 600 K	0.07045	0.04204	0.00296
T_w = 800 K	0.07600	0.04680	0.00351
T_w = 1000 K	0.05786	0.04014	0.00403

4. Conclusion

In this study, discrete particle model (DPM) in ANSYS FLUENT is selected to simulate droplet lateral movement and deposition behaviors in post-dryout region. A variety of methods are utilized a to analyze droplet lateral movement, including tracking individual droplet trajectories, performing statistical analyses of droplet behaviors, and evaluating overall mass flux through three novel parameters—droplet deposition mass flux, droplet deposition velocity, and droplet entrainment velocity—enabling a quantitative and comprehensive exploration of droplet dynamics in the post-dryout region. In addition, effect of droplet evaporation on the droplet deposition behavior under various wall temperatures are investigated. Main conclusions are summarized as below:

- The distribution of droplets radial velocities showed the droplets with positive radial velocities follows a normal distribution along the positive semi-axis. No clear statistical pattern was observed along the negative semi-axis due to the presence of numerous droplets with small negative radial velocities. A comparison of cases with different droplet sizes reveals that smaller droplets result in higher average radial velocities toward the wall, indicating that droplet lateral movement is highly sensitive to droplet size. The droplet deposition model in post-dryout region should consider the droplet size effect well.
- Comparing the cases with and without evaporation reveals that the number of droplets with low radial velocities towards the wall is significantly reduced in the case with evaporation, whereas the number of droplets with low radial velocities towards tube centre increases. Through stopping the droplets with small positive radial velocities, the evaporation reduces the overall droplet deposition mass flux from the central region to the near wall region.
- In addition to the droplet individual velocity, three new parameters presenting overall movement behavior, i.e. droplet deposition mass flux, droplet deposition velocity as well as droplet entrainment velocity are introduced and derived from the CFD results. By catching the droplets moving across the boundary between the central region and the near wall region, the effects of droplet size and droplet evaporation on droplet deposition and entrainment can be quantitatively demonstrated.
- Evaporation in the near wall region tends to inhibit the movement of droplets towards the wall while promoting droplets back to the main flow. The higher the wall temperature or the greater the evaporation intensity, the more pronounced is the effect of inhibiting deposition and promoting entrainment. This indicates that droplet lateral movement is significantly influenced by evaporation, especially under high evaporation intensity. As a result, deposition correlations

from unheated walls are deemed inapplicable to post-dryout regions, highlighting the necessity for a new deposition model tailored to the conditions with the existence of droplet evaporation.

From the current simulation, it was found that the droplet evaporation can have strong effect on droplet deposition behaviors, which indicates that taking the deposition correlations from the unheated conditions are not suitable for the droplet deposition calculation in the post-dryout region. Besides, the droplet size is also found has impact on droplet deposition. In the future, a new droplet deposition models that accounts for evaporation and size effects could be developed. Given the significance of droplet lateral movement in interfacial heat transfer, this deposition model could be integrated into interfacial heat transfer models for post-dryout heat transfer prediction.

On the other hand, the DPM method employed in this study is suitable for simulating scenarios where the droplet volume fraction is below 10 %. However, for post-dryout heat transfer conditions where the droplet volume fraction exceeds 10 %, the current method is no longer applicable. In such cases, the DDPM (Dense Discrete Phase Model), a Euler-Euler-Lagrange approach, could be considered for future work. Moreover, when the droplet volume fraction is high, collisions between droplets need to be carefully accounted for.

CRediT authorship contribution statement

Zihan Xia: Investigation, Conceptualization, Methodology, Writing – original draft, Data curation, Formal analysis, Validation, Software, Visualization. **Xu Cheng:** Supervision, Writing – review & editing, Funding acquisition, Project administration, Resources.

Declaration of competing interest

The authors declare that they have no known competing financial interests or personal relationships that could have appeared to influence the work reported in this paper.

Acknowledgments

This work is sponsored by the German Federal Ministry of Education and Research (BMBF) under the contract number 02NUK062. The partial financial support for the first author through China Scholarship Council (CSC) is highly appreciated. Responsibility for the content of this report lies with the authors.

Data availability

Data will be made available on request.

References

[1] Y. Jin, F. Cheung, S.M. Bajorek, K. Tien, C.L. Hoxie, Development of a two-phase flow mass quality correlation in the post-dryout DFFB regime during reflood transients, Int. J. Heat. Mass Transf. 137 (2019) 1076–1087.
[2] W. Fan, H. Li, H. Anglart, A study of rewetting and conjugate heat transfer influence on dryout and post-dryout phenomena with a multi-domain coupled CFD approach, Int. J. Heat. Mass Transf. 163 (2020) 120503.
[3] D. Yu, C. Xu, C. Hu, Y. Fan, Universal approach to predicting full-range post-dryout heat transfer under uniform and non-uniform axial heat fluxes, Nucl. Eng. Des. 393 (2022) 111790.
[4] M. Chen, H. Liu, H. Liu, L. Zhong, J. Deng, Q. Zuo, J. Wu, D. Chen, Experimental study on heat transfer characteristics of dispersed flow during strong transient reflood process, Int. J. Heat. Mass Transf. 228 (2024) 125655.
[5] K. Yang, K. Jin, J.i Xiong, Y.o Luo, Y. Liang, C. Liu, Interfacial heat transfer and boiling transition of the droplets on superheated surface with Leidenfrost effects, Int. J. Heat. Mass Transf. 212 (2023) 124297.
[6] N. Saini, I.A. Bolotnov, Two-phase turbulence statistics from high fidelity dispersed droplet flow simulations in a pressurized water reactor (PWR) sub-channel with mixing vanes, Fluids 6 (2) (2021) 72.
[7] M. Chen, D. Chen, H. Liu, H. Liu, L. Zhong, J. Deng, Experimental investigation of droplet transient behavior during reflood cooling process of single-rod channel, Int. J. Therm. Sci. 195 (2024) 108667.
[8] A.F. Varone, W.M. Rohsenow, Post dryout heat transfer prediction, Nucl. Eng. Des. 95 (1986) 315–327.
[9] O.C. Iloeje, W.M. Rohsenow, P. Griffith, Three-step model of dispersed flow heat transfer (Post CHF vertical flow), Niger. J. Technol. 13 (1) (1989) 1–15.
[10] J.M. Meholic, The Development of a Non-Equilibrium Dispersed Flow Film Boiling Heat Transfer Modelling Package, The Pennsylvania State University, 2011. Ph. D. thesis.
[11] S.K. Friedlander, H.F. Johnstone, Deposition of suspended particles from turbulent gas streams, Ind. Eng. Chem. 49 (1957) 1151–1156.
[12] B.Y. Liu, T.A. Ilori, Aerosol deposition in turbulent pipe flow, Environ. Sci. Technol. 8 (4) (1974) 351–356.
[13] G.A. Sehmel, Aerosol Deposition from Turbulent Airstreams in Vertical Conduits, Rep. BNWL-578, Batelle Northwest Lab, Richland, Washington, 1968.
[14] Y. Guo, K. Mishima, A non-equilibrium mechanistic heat transfer model for post-dryout dispersed flow regime, Exp. Therm. Fluid. Sci. 26 (2002) 861–869.
[15] S. Talebi, H. Kazeminejad, H. Davilu, Prediction of dryout and post-dryout wall temperatures using film thickness model, Nucl. Eng. Des. 244 (2012) 73–82.
[16] I. Kataoka, M. Ishii, A. Nakayama, Entrainment and deposition rates of droplets in annular two-phase flow, Int. J. Heat. Mass Transf. 43 (9) (2000) 1573–1589.
[17] G.F. Hewitt, A.H. Govan, Phenomenological modelling of non-equilibrium flows with phase change, Int. J. Heat. Mass Transf. 33 (2) (1990) 229–242.
[18] I.I. Paleev, B.S. Filippovich, Phenomena of liquid transfer in two-phase dispersed annular flow, Int. J. Heat. Mass Transf. 9 (10) (1966) 1089–1093.
[19] R.A. Farmer, Liquid Droplet Trajectories in Two-Phase Flow, Massachusetts Institute of Technology. Dept. of Nuclear Engineering, 1969. Ph. D. thesis.
[20] P. Andreussi, Droplet transfer in two-phase annular flow, Int. J. Multiph. Flow 9 (6) (1983) 697–713.
[21] K. Mastanaiah, E.N. Ganic, Surface effect on droplet deposition in two-phase flow, Int. J. Heat. Mass Transf. 25 (3) (1982) 422–424.
[22] E. Ganic, K. Mastanaiah, Investigation of droplet deposition from a turbulent gas stream, Int. J. Multiph. Flow 7 (1981) 401–422.
[23] Z.H. Yang, S.L. Lee, On the droplet deposition and mist supercooling in a turbulent channel flow, particle & particle systems characterization, 8 (1991) 72–78.
[24] E.A. Matida, K. Torii, Droplet deposition and heat transfer simulations of turbulent air-water dispersed flow in a vertical tube, JSME Int. J. Ser. B Fluids Therm. Eng. 38 (4) (1995) 628–636.
[25] R.A. Moose, E.N. Ganic, On the calculation of wall temperatures in the post dryout heat transfer region, Int. J. Multiph. Flow 8 (5) (1982) 525–542.
[26] M.J. Meholic, D.L. Aumiller, F.B. Cheung, A comprehensive, mechanistic heat transfer modeling package for dispersed flow film boiling - part 1 – development, Nucl. Eng. Des. 291 (2015) 295–301.
[27] S.K. Beal, Deposition of particles in turbulent flow on channel or pipe walls, Nucl. Sci. Eng. 40 (1) (1970) 1–11.
[28] W. Köhler, D. Hein, Influence of the wetting state of a heated surface on heat transfer and pressure loss in an evaporator tube, in: Technical Report NUREG/IA-0003, Nuclear Regulatory Commission, Washington, DC (USA), Office of Nuclear Regulatory Research; Kraftwerk Union AG, Erlangen (Germany, FR), 1986.
[29] G. Kendall, W. Rohsenow, Heat Transfer to Impacting Drops and Post Critical Heat Flux Dispersed Flow, Heat Transfer Laboratory, Dept. of Mechanical Engineering, Cambridge, MA, 1978. Technical Report MIT-56987-100.
[30] A. Bennett, G. Hewitt, H. Kearsey, R. Keeys, Heat Transfer to Steam-Water Mixtures Flowing in Uniformly Heated Tubes in Which the Critical Heat Flux Has Been Exceeded, Atomic Energy Research Establishment, Harwell, Eng, 1967. Technical Report REP/AERE-R-5373.
[31] W. Laverty, W. Rohsenow, Film Boiling of Saturated Liquid Flowing Upward Through a Heated Tube: High Vapor Quality Range, MIT Dept. of Mechanical Engineering, Cambridge, MA, 1964. Technical Report 9857-32.
[32] P. Saha, A nonequilibrium heat transfer model for dispersed droplet post-dryout regime, Int. J. Heat. Mass Transf. 23 (1980) 483–492.
[33] Z. Xia, X. Cheng, W. Liu, CFD simulation on droplet behaviour in post-dryout region, Kerntechnik 89 (2024) 124–132.
[34] D.D. McCoy, T.J. Hanratty, Rate of deposition of droplets in annular two-phase flow, Int. J. Multiph. Flow 3 (1977) 319–331.
[35] E.A. Matida, K. Nishino, K. Torii, Statistical simulation of particle deposition on the wall from turbulent dispersed pipe flow, Int. J. Heat. Fluid. Flow. 21 (2000) 389–402.
[36] J. Zhang, A. Li, CFD simulation of particle deposition in a horizontal turbulent duct flow, Chem. Eng. Res. Des. 86 (2008) 95–106.
[37] N. Gao, J. Niu, Q. He, T. Zhu, J. Wu, Using RANS turbulence models and Lagrangian approach to predict particle deposition in turbulent channel flows, h to predict particle deposition in turbulent channel flows, Build. Environ. 48 (2012) 206–214.
[38] C. Lo, J. Bons, Y. Yao, J. Capecelatro, Assessment of stochastic models for predicting particle transport and deposition in turbulent pipe flows, J. Aerosol. Sci. 162 (2022) 105954.
[39] S. Aguinaga, O. Simonin, J. Borée, V. Herbert, A. Lagrangian, Stochastic model for droplet deposition simulations in connection with wall function approaches, in: Proceedings of the ASME 2009 Fluids Engineering Division Summer Meeting, Volume 1: Symposia, Parts A, B and C, Vail, Colorado, USA, ASME, 2009, pp. 795–805. August 2–6.
[40] ANSYS Fluent Theory Guide 2021 R1, ANSYS, Inc., Canonsburg, 2021.
[41] S.A. Morsi, A.J. Alexander, An investigation of particle trajectories in two-phase flow systems, J. Fluid. Mech. 55 (1972) 193–208.
[42] F. Akao, K. Araki, S. Mori, A. Moriyama, Deformation behaviors of a liquid droplet impinging onto hot metal surface, Trans. Iron Steel Inst. Japan 20 (1980) 737–743.

[43] F. Birkhold, Selektive Katalytische Reduktion von Stickoxiden in Kraftfahrzeugen: Untersuchung der Einspritzung von Harnstoffwasserlösung, University of Karlsruhe, 2007, p. 541. Dissertation.

[44] K.M. Becker, C.H. Ling, S. Hedberg, G. Strand, An Experimental Investigation of Post Dryout Heat Transfer, KTH, Stockholm, Sweden, 1983. Report KTH-NEL-33.

[45] T. Ueda, K. Kim, Dryout heat flux and size of entrained drops in a flow boiling system, Bull. JSME 25 (1982) 225–233.